Transformation of Bimetal Carboxylate-MOF into Phosphonate-based MOF as Multifunctional Photocatalyst

Aihui Cao[a], *Kang Li*[b,c], *Xiao Xu*[b,c], *Longtian Kang*[b,c] *and Min Zhang*[d,e]*

[a] Key Laboratory of Catalysis Science and Technology of Chongqing Education Commission, Chongqing Key Laboratory of Catalysis and New Environmental Materials, College of Environmental and Resources, Chongqing Technology and Business University, Chongqing, 400067, China.
*Corresponding author. E-mail: caoaihui137@ctbu.edu.cn. (Aihui Cao)
[b] Key Laboratory of Design and Assembly of Functional Nanostructures, and Fujian Provincial Key Laboratory of Nanomaterials, Fujian Institute of Research on the Structure of Matter, Chinese Academy of Sciences, Fuzhou, Fujian 350002, P. R. China.
[c] Fujian Science & Technology Innovation Laboratory for Optoelectronic Information of China, Fuzhou, Fujian 350108, P. R. China.
[d] Institute of Engineering Thermophysics, School of Energy and Power Engineering, Chongqing University, Chongqing, 400044, P. R. China.
*Corresponding author. E-mail: zhangmin2022@cqu.edu.cn (Min Zhang)
[e] Key Laboratory of Low-grade Energy Utilization Technologies and Systems, Chongqing University, Ministry of Education, Chongqing 400044, China.

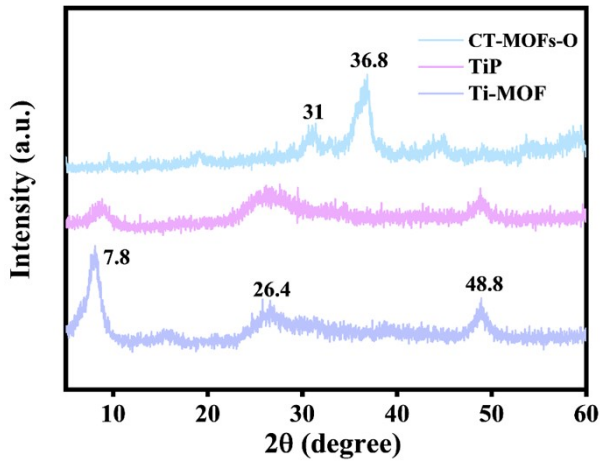

Figure S1. XRD pattern of Ti-MOF, TiP and CT-MOFs-O.

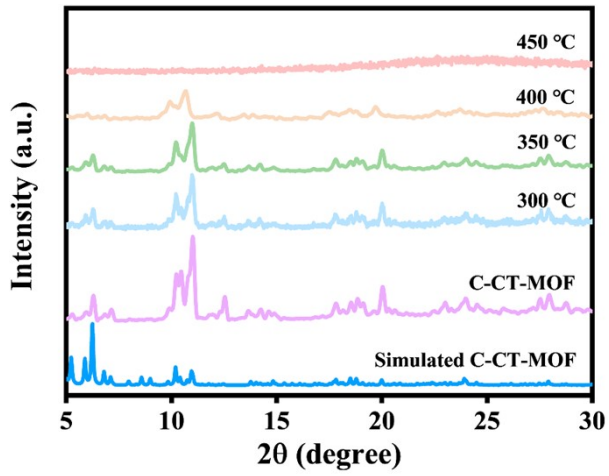

Figure S2. XRD pattern of C-CT-MOF with different temperature.

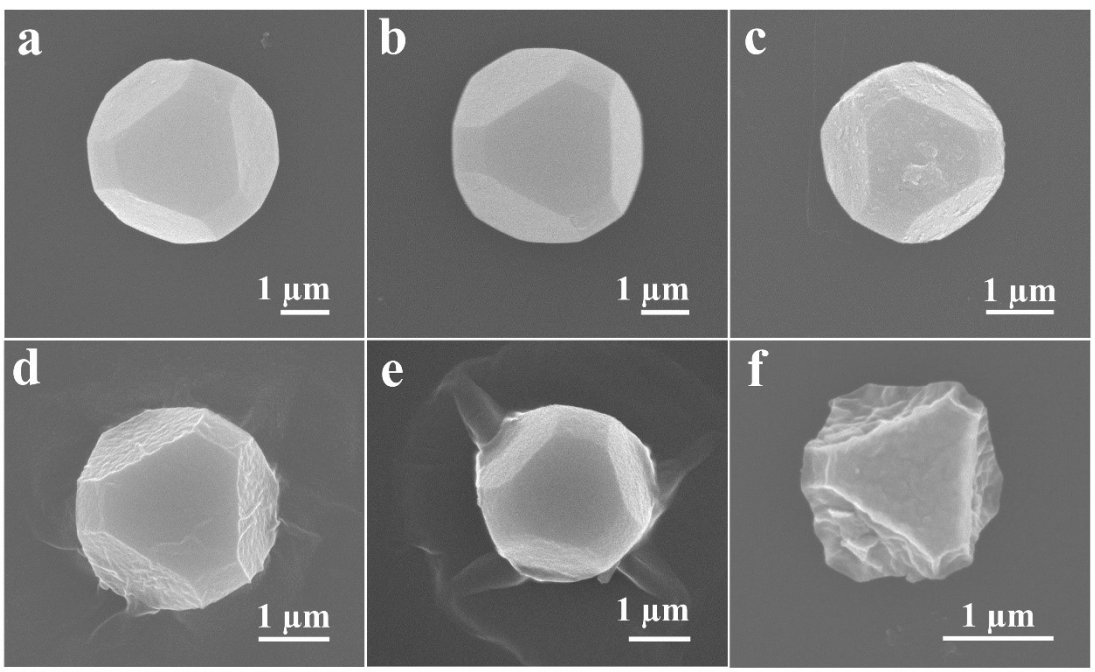

Figure S3. SEM images of (a) C-CT-MOF with different calcined temperature, (b) 300℃, (c) 350℃, (d) 400℃, (e) 450℃ and (f) 350℃ with O_2 atmosphere.

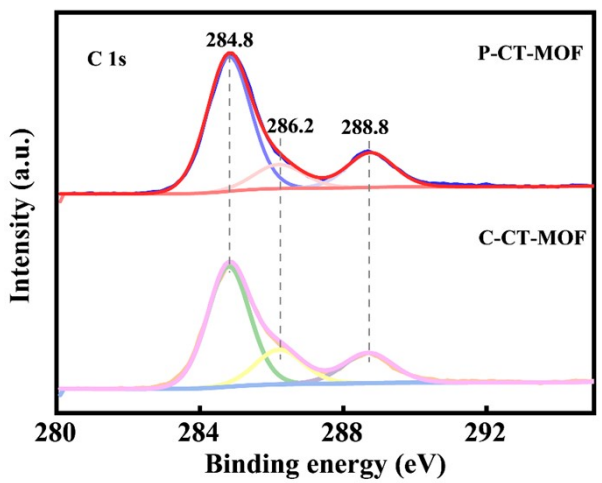

Figure S4. High resolution XPS spectra of C 1s of C-CT-MOF and P-CT-MOF.

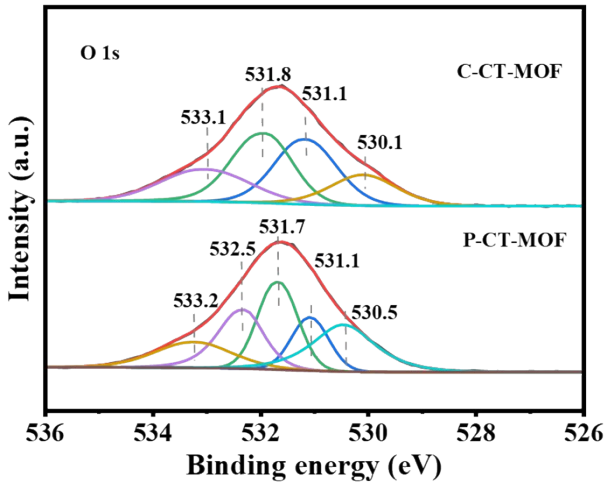

Figure S5. High resolution XPS spectra of O 1s of C-CT-MOF and P-CT-MOF.

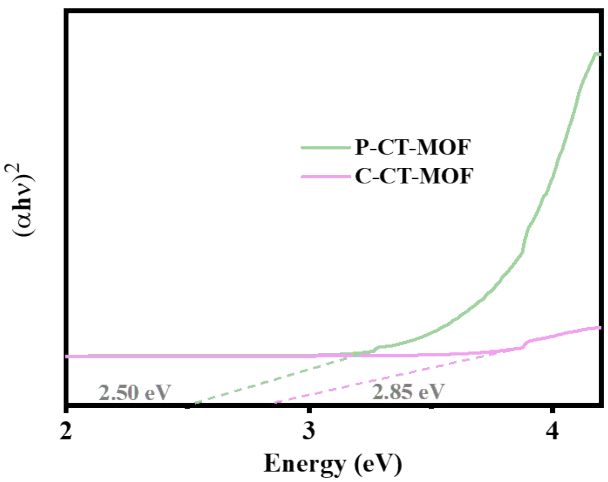

Figure S6. The band gap of C-CT-MOF and P-CT-MOF.

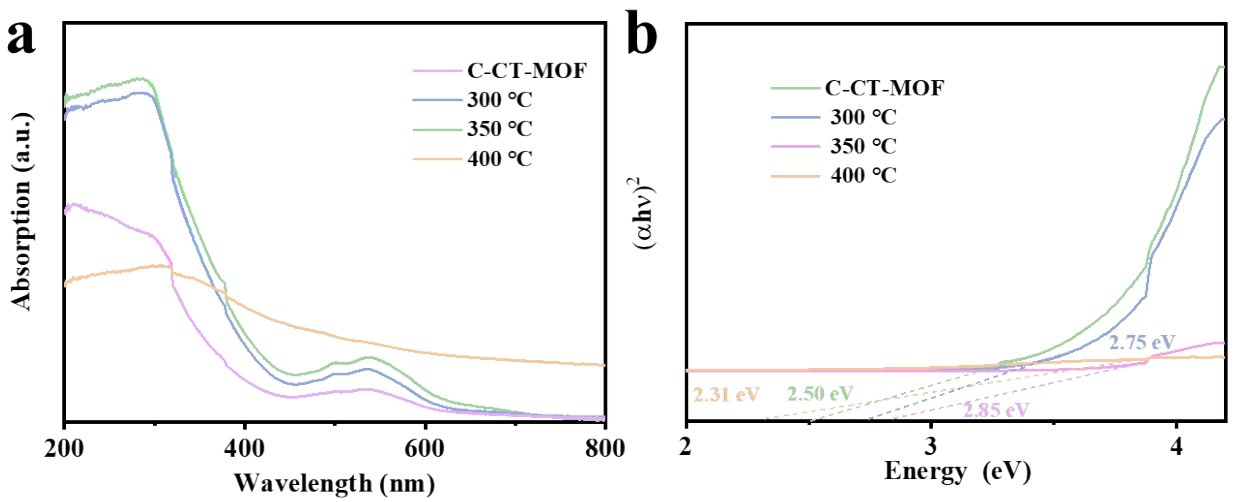

Figure S7. The UV-vis DRS and the band gap of C-CT-MOF and P-CT-MOF at different calcination temperature.

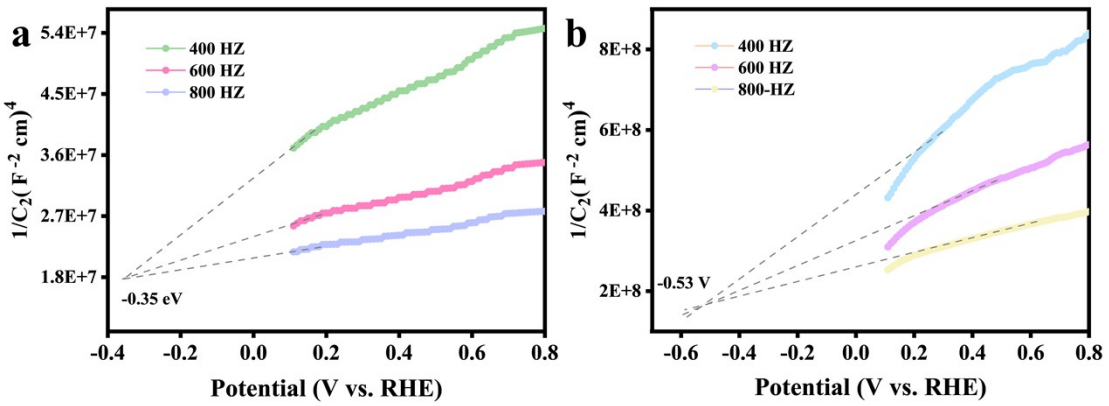

Figure S8. M-S curve plot of C-CT-MOF and P-CT-MOF.

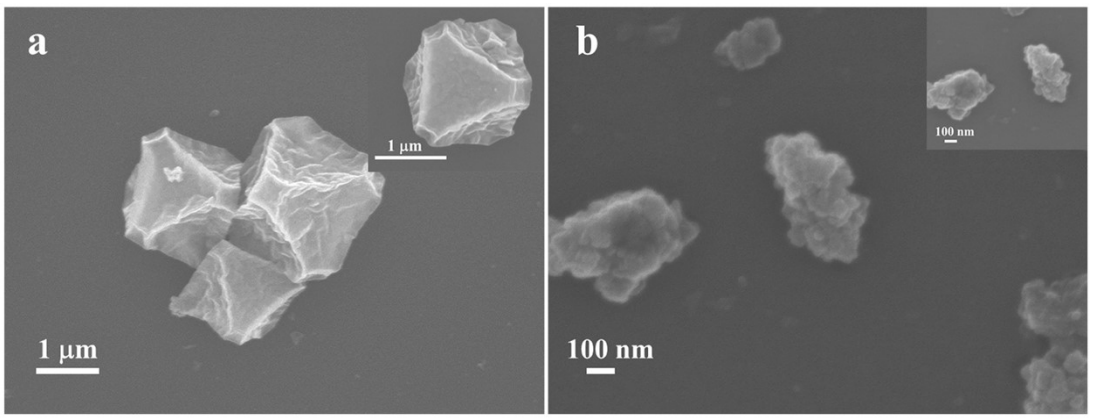

Figure S9. The SEM image of CT-MOFs-O and Ti-MOF.

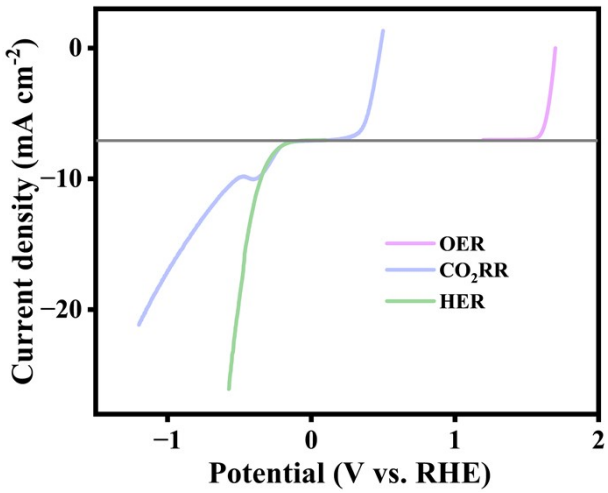

Figure S10. LSV curves in Electrocatalytic OER, HER and CO_2RR of P-CT-MOF.

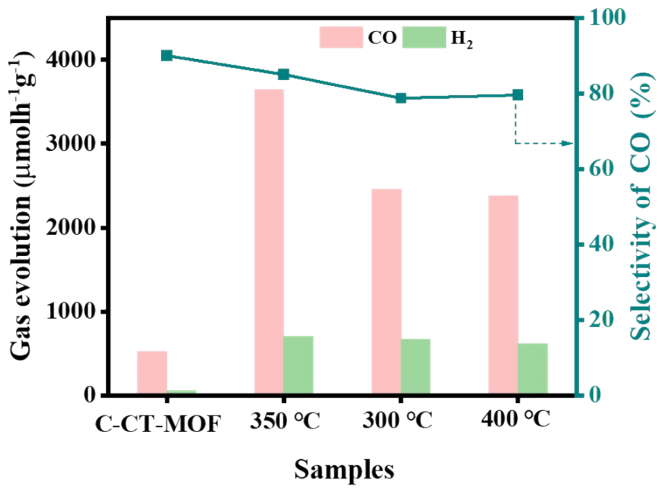

Figure S11. The Photocatalytic CO_2RR performance of samples at different calcination temperature.

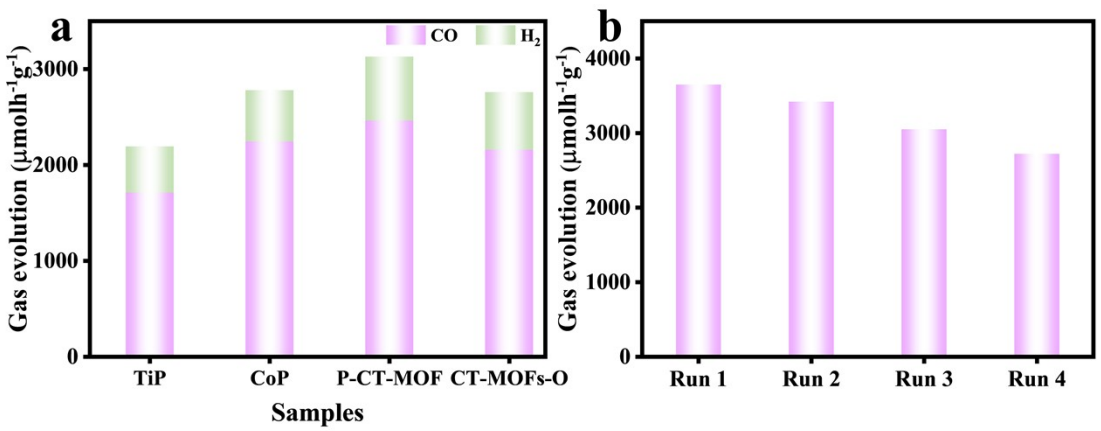

Figure S12. The Photocatalytic CO_2RR performance of samples at (a) different

catalyst and (b) run stability.

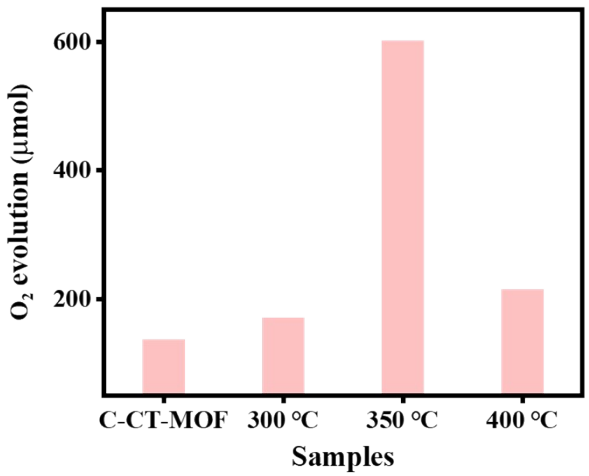

Figure S13. The Photocatalytic OER performance of samples at different calcination temperature.

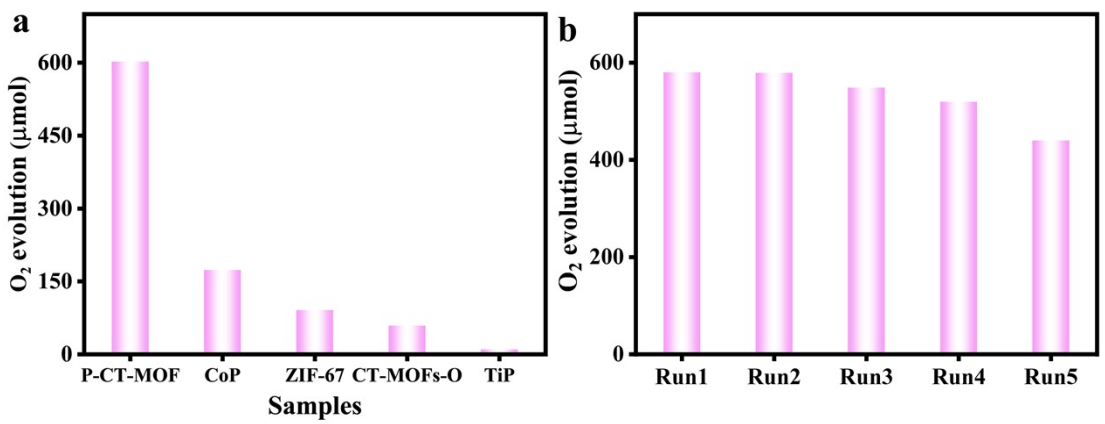

Figure S14. The photocatalytic OER performance of (a) different samples and (b) run stability.

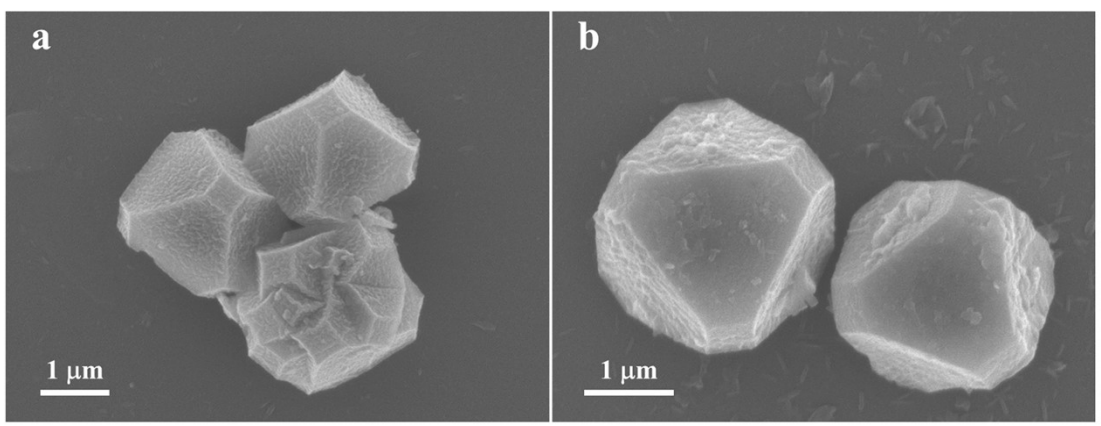

Figure S15. The SEM image of P-CT-MOF after photocatalytic CO_2RR.

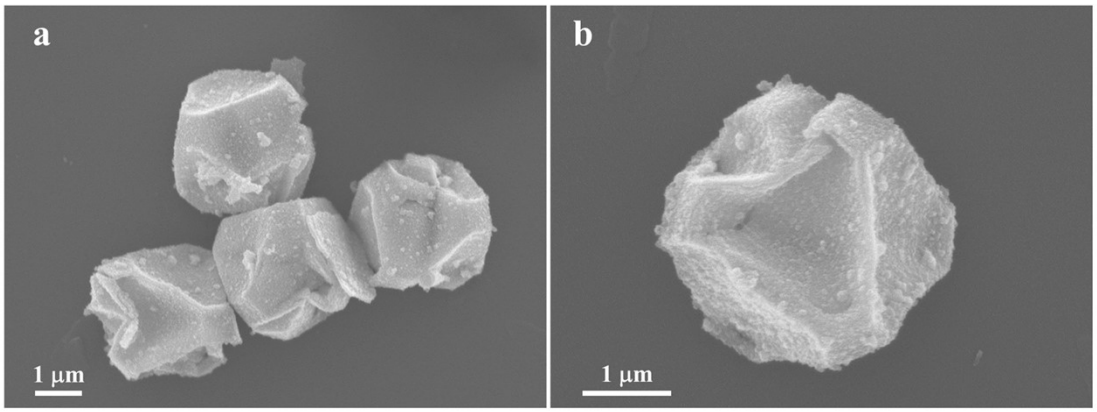

Figure S16. (a, b) The SEM image of P-CT-MOF after photocatalytic OER.

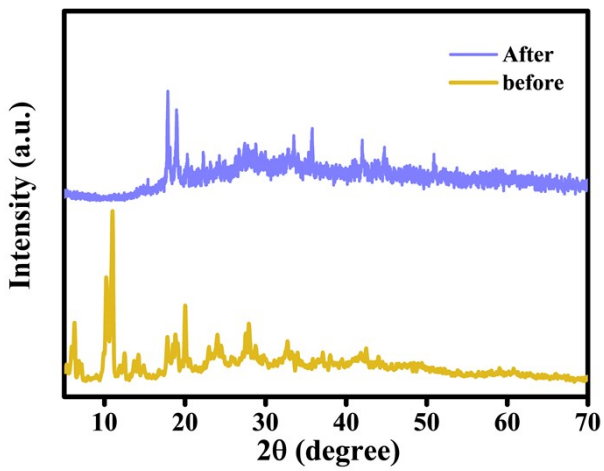

Figure S17. The XRD pattern of P-CT-MOF before and after photocatalytic CO_2RR.

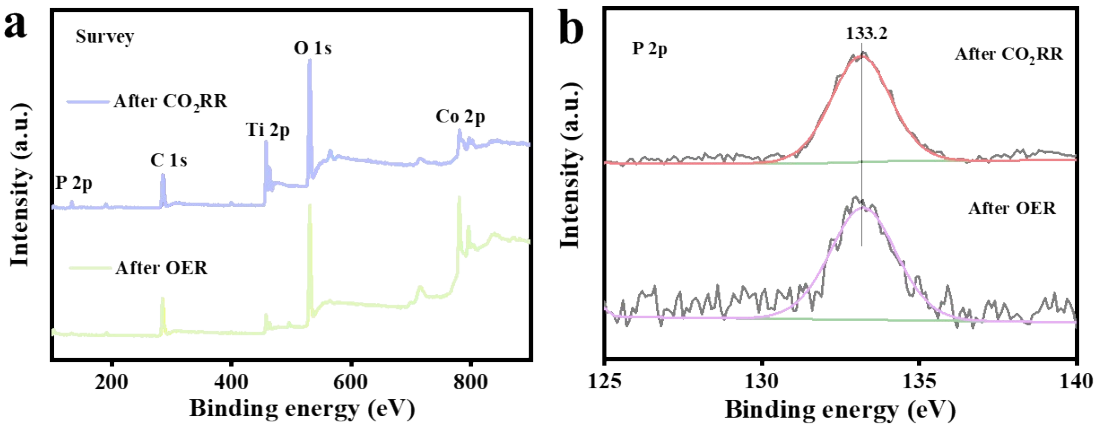

Figure S18. (a) The XPS full survey spectra and (b) P 2p spectra of after photocatalytic CO_2RR and OER of P-CT-MOF samples.

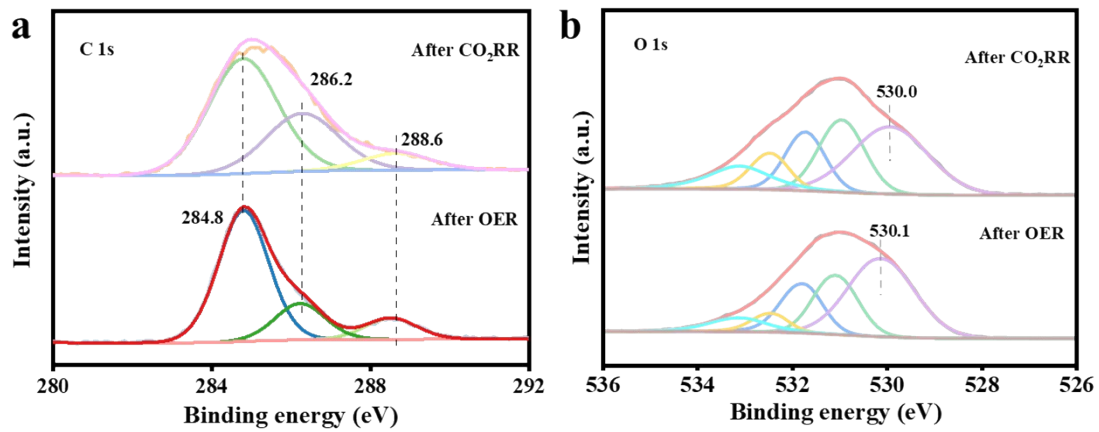

Figure S19. The XPS spectra of after photocatalytic CO_2RR and OER of P-CT-MOF samples; (a) C 1s, (b) O 1s.

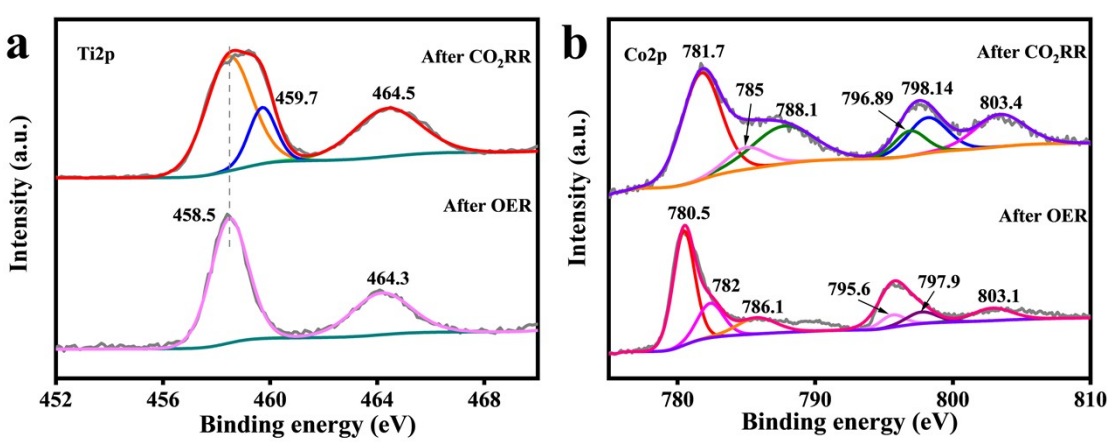

Figure S20. The SEM (a, b) and XPS (c, d) spectra after photocatalytic CO_2RR and OER of P-CT-MOF samples (c) Ti 2p and (d) Co 2p.

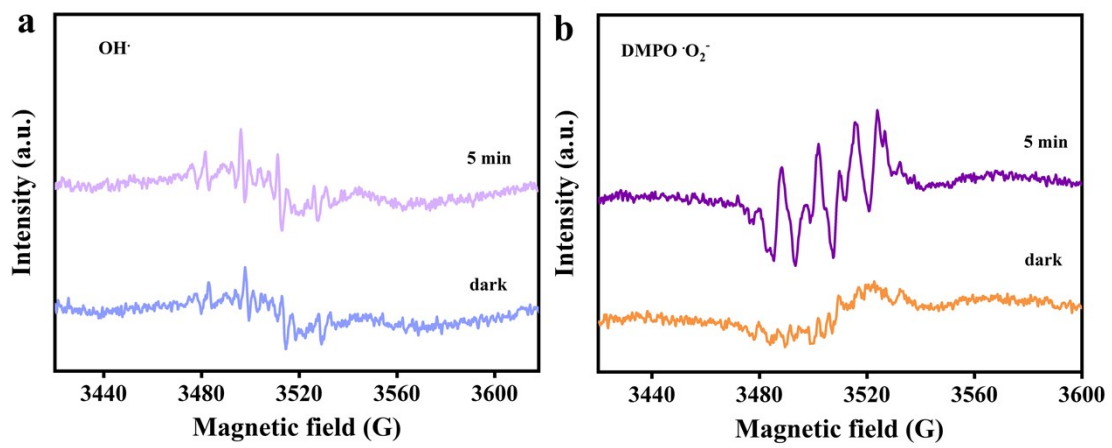

Figure S21. EPR of C-CT-MOF in aqueous solution and methanol solution.

Table S1. The composition of P-CT-MOF by ICP-OES before and after CO_2RR

reaction.

P-CT-MOF	before	after
Co:Ti (%)	14.37:8.80	11.40: 6.90

Table S2. Comparison table of photocatalytic activity of semiconductor catalysts for CO_2RR.

Materials	λ	CO rate(μmolh^{-1}g^{-1})	AQY	literature
P-CT-MOF	λ≥ 420 nm	3650.3	no	Our work
NiMOF/g-C_3N_4	λ≥ 420 nm	54.5	no	[1]
FeOOH/CdS	λ≥ 420 nm	12.55	4.6	[2]
Re(I)MOF	λ≥ 420 nm	1070	1.97	[3]
Au-NC@UiO-68NH_4	λ≥ 400 nm	57.6	no	[4]
Re-UiO-67	λ≥ 400 nm	412.5	no	[5]
MnMOF	λ≥ 420 nm	21	no	[6]
NH_2-TiMOF	λ≥ 420 nm	100.46	no	[7]
MIL-101(Fe)	λ≥ 400 nm	11.5	0.943	[8]
UiO-67-Re	λ≥ 420 nm	60.6	no	[9]
ZrMOF	λ≥ 420 nm	1920	no	[10]
TiO_2/NiIP NSs	λ≥ 420 nm	54.9 mmol g^{-1}h^{-1}	no	[11]
InTCPP	λ≥ 420 nm	61.2	no	[12]
CoIn-LDH/MOF	λ≥ 420 nm	2320	no	[13]
Zr-NDI@Ru-tpy	λ≥ 420 nm	2449	no	[14]
CoTiPa	λ≥ 420 nm	49.92	2.05	[15]

Literature

[1] Zhao L, Zhao Z, Li Y, et al. The Synthesis of Interface-Modulated Ultrathin Ni(ii) MOF/g-C_3N_4 Heterojunctions as Efficient Photocatalysts for CO_2 Reduction[J]. Nanoscale, 2020, 12: 10010-

10018.

[2] Li L, Guo C, Ning J, et al. Oxygen-Vacancy-Assisted Construction of FeOOH/CdS Heterostructure as an Efficient Bifunctional Photocatalyst for CO_2 Conversion and Water Oxidation[J]. Applied Catalysis B: Environmental, 2021, 293:120203.

[3] Choi S, Jung W, Park K, et al. Rapid Exciton Migration and Amplified Funneling Effects of Multi-Porphyrin Arrays in a Re(I)/Porphyrinic MOF Hybrid for Photocatalytic CO_2 Reduction[J]. ACS Applied Materials Interfaces, 2021, 13: 2710-2722.

[4] Jiang Y, Yu Y, Zhang X, et al. N-Heterocyclic Carbene-Stabilized Ultrasmall Gold Nanoclusters in a Metal-Organic Framework for Photocatalytic CO_2 Reduction[J]. Angewandte Chemie International Edition, 2021, 60: 17388-17393.

[5] Gao X, Guo B, Guo C, et al. Zirconium-Based Metal-Organic Framework for Efficient Photocatalytic Reduction of CO_2 to CO: The Influence of Doped Metal Ions[J]. ACS Applied Materials Interfaces, 2020, 12: 24059-24065.

[6] Qin J, Xu P, Huang Y, et al. High Loading of Mn(ii)-Metalated Porphyrin in a MOF for Photocatalytic CO_2 Reduction in Gas-Solid Conditions[J]. Chemical communication, 2021, 57: 8468-8471.

[7] Cheng X, Zhang X, Dao X, et al. High-Index Facets Exposed on Metal–Organic Framework for Boosting Photocatalytic Carbon Dioxide Reduction[J]. Chemical Engineering Journal, 2022, 431: 134125.

[8] Dao X, Guo J, Zhang X, et al. Structure-Dependent Iron-Based Metal–Organic Frameworks for Selective CO_2-to-CH_4 Photocatalytic Reduction[J]. Journal of Materials Chemistry A, 2020, 8: 25850-25856.

[9] Nakajima T, Tamaki Y, Ueno K, et al. Photocatalytic Reduction of Low Concentration of CO_2[J]. Journal of the American Chemical Society, 2016, 138: 13818-13821.

[10] Li M, Li C, Shi Y, Zhang H, Fan Z, Liu Y, Zhang J, Pang J. and Bu X, et al. Embedding Metallosalen Active Sites in Zr-MOF for Enhanced Selective Syngas Production from CO_2 Photoreduction [J]. Angewandte Chemie International Edition, 2025, 137, e202510810.

[11] Wu C, Song K, Zhang X, Tan B, Liao R, Liu Z, Zhu H, Wang J, et al. Highly Efficient Photocatalytic CO_2-to-CO on Ni-Based Cationic Polymer with TiO_2-Assisted Exfoliation and Stabilization[J]. Angewandte Chemie International Edition, 2025, 64, e202423200.

[12] Cai Z, Liu H, Dai J, Li B, Yang L, Wang J, Zhu H, et al. Sunlight-driven simultaneous CO_2 reduction and water oxidation using indium-organic framework heterostructures[J]. Nature Communications, 2025, 16, 2601.

[13] Feng J, Li W, Chen T, Zeng Z, Tian M, Ji W, Guo Y, Min S, Liu X, et al. Co–In Bimetallic Hydroxide Nanosheet Arrays with Coexisting Hydroxyl and Metal Vacancies Anchored on Rod-Like MOF Template for Enhanced Photocatalytic CO_2 Reduction[J]. Advanced Science, 12, e2411673.

[14] Jana A, Maity A, Adalder A, Saha S, Bhunia A, et al. A molecularly engineered MOF photocatalyst for CO production from visible light-driven CO_2 reduction[J]. Nanoscale, 17, 12235-12244.

[15] Chen Y, Hsieh N, Hsu, S W, et al. Plasmonic Nanocrystal-MOF Nanocomposites as Highly Active Photocatalysts and Highly Sensitive Sensors for CO_2 Reduction over a Wide Range of Solar Wavelengths[J]. Small Methods, 2025,19, e2500081.